Title: Shear crack growth in brittle materials modeled by constrained Cosserat elasticity

Author: Panos A. Gourgiotis

PII: S0955-2219(17)30865-8
DOI: https://doi.org/doi:10.1016/j.jeurceramsoc.2017.12.056
Reference: JECS 11661

To appear in: *Journal of the European Ceramic Society*

Received date: 27-11-2017
Revised date: 23-12-2017
Accepted date: 25-12-2017

Please cite this article as: Panos A. Gourgiotis, Shear crack growth in brittle materials modeled by constrained Cosserat elasticity, *<![CDATA[Journal of the European Ceramic Society]]>* (2017), https://doi.org/10.1016/j.jeurceramsoc.2017.12.056

Shear crack growth in brittle materials modeled by constrained Cosserat elasticity

Panos A. Gourgiotis*

Department of Engineering, Durham University,
South Road, Durham, DH1 3LE, UK

Abstract

The propagation of in-plane shear cracks is investigated in brittle microstructured materials modeled by the constrained Cosserat elasticity. This theory introduces characteristic material lengths in order to describe the scale effects that emerge from the underlying microstructure and has proved to be very effective for modeling complex microstructured materials. An exact solution is obtained based on integral transforms and the Wiener-Hopf technique. Numerical results are presented illustrating the dependence of the stress intensity factor and the energy release rate upon the loading profile, the propagation velocity, and the characteristic material lengths of Cosserat elasticity. It is shown that depending on the Cosserat microstructural lengths the limiting crack propagation velocity can be significantly lower than the classical Rayleigh limit. Moreover, strengthening effects are observed when the characteristic material lengths become comparable to the geometrical lengths of the problem, a behavior that has been experimentally verified in fracture of ceramics.

Keywords: Dynamic fracture; Couple-stress elasticity; Microstructure; Mode-II crack; Micro-rotational inertia; Ceramics; Limiting crack velocity

1. Introduction

Brittle materials such as ceramics, foams, glassy, and semi-crystalline polymers are inherently heterogeneous materials possessing microstructures at different scales which affect strongly their effective properties (see e.g. [1]). Due to their intrinsinc microstructure such materials exhibit size effects during deformation especially in the presence of large stress (or strain) gradients [2]. In the last decade, brittle fracture in heterogeneous materials has received significant attention, especially in the dynamical case where many fundamental questions regarding the limiting crack-tip velocity, velocity-toughening mechanisms, and crack branching still remain unanswered [3, 4]. During brittle fracture, the microstructural morphology and the associated size effects play a dominant role in determining the

*Corresponding author: Panos Gourgiotis, panagiotis.gourgiotis@durham.ac.uk

macroscopic fracture toughness of these materials [5, 6]. The influence of heterogeneities in dynamic fracture processes has been investigated across various length scales, ranging from kilometers for earthquakes [7, 8], to millimeters for composite plates [9] and thin-films [10], to micro/nanometers in ceramics and metallic glasses [5, 11, 12, 13, 14]. The majority of such investigations are based on the classical theory of linear elastic fracture mechanics (LEFM) which, however, is scale independent and cannot realistically describe the fracture processes in such situations. This deficiency of the classical theory can be circumvented by the use of generalized continuum theories. These theories introduce characteristic material lengths in their formulation and have been used successfully to model the experimentally observed size-effects in many cases. It is worth noting that another approach in the continuum setting to introduce appropriate length scales connected to submacroscopic geometrical changes is through the use of the multiscale geometry of structured deformations [15] which is a generalization of the theory of structured deformations [16, 17].

One of the most effective generalized continuum theories has proved to be the theory of constrained Cosserat elasticity also known as couple-stress elasticity [18, 19, 20]. This theory is the simplest gradient theory in which couple-stresses make their appearance. In particular, the constrained Cosserat theory assumes an augmented form of the Euler-Cauchy principle with a non-vanishing couple traction, and a strain-energy density that depends upon both the strain and the gradient of rotation. Such assumptions are appropriate for materials with granular or cellular structure, where the interaction between adjacent elements may introduce internal moments. For the isotropic case, the constrained Cosserat theory introduces material length scales which can be related to the intrinsic material microstructure [21, 22, 23, 24]. The constrained Cosserat theory has been recently employed successfully to model size effects in microstructured materials in, among other areas, fracture [25, 26, 27, 28, 29, 30, 31], contact [32, 33, 34], stress localization [35, 36, 37, 38], and wave propagation problems [39, 40, 41, 42].

The present work deals with the problem of mode II crack propagating steadily with sub-Rayleigh velocity in a constrained Cosserat medium. Both inertia and micro-inertia terms are taken into account in the analysis. The inclusion of the micro-inertia term is crucial in our problem since it provides one additional length scale and gives dispersion curves that mostly resemble with the ones obtained by atomic-lattice considerations [43, 44, 28]. The main goal of the present work is to investigate how different loading cases can affect the energetics of the fracture process. In this context, the work of Gourgiotis and Piccolroaz [28] is extended here to consider more general loading profiles. A full field exact solution of the boundary value problem is obtained by means of the Fourier transform and the Wiener-Hopf technique. To define the range of the sub-Rayleigh regime, we examine also the propagation of Rayleigh surface waves in an elastic constrained Cosserat half-plane. It is shown that the present theory can indeed predict the dispersive character of Rayleigh waves in a medium with microstructure. Moreover, depending on the material microstructure the limiting crack propagation velocity can be

significantly lower than the classical Rayleigh limit. The latter finding verifies observations in shear fault ruptures where the limiting velocity varies in the range $0.7 \sim 0.9$ of the shear wave velocity ([4],[7]). Further, closed-form expressions for the stress intensity factor (SIF) and the dynamic energy release rate (ERR) are obtained. The dependence of these quantities upon the crack speed, the characteristic material lengths of the theory, and the loading profile is then examined in detail. A comparison of these quantities in the framework of couple-stress elasticity with the classical elasticity solutions (which are also obtained in closed form herein) reveals an interesting 'alternating' behavior between strengthening and weakening effects depending on the distance of the maximum value of the shear traction to the crack-tip as compared to the characteristic Cosserat lengths.

2. Basic equations of plane-strain constrained Cosserat elasticity

In this section, we recall briefly the pertinent elements of the dynamic plane strain constrained Cosserat elasticity (also known as couple-stress elasticity). A thorough presentation of the three dimensional dynamic anisotropic constrained Cosserat theory including micro-inertial effects can be found in [42].

For a body that occupies a domain in the (x, y)-plane under conditions of plane strain, the displacement field takes the general form

$$u_x \equiv u_x(x, y, t) \neq 0, \quad u_y \equiv u_y(x, y, t) \neq 0, \quad u_z \equiv 0. \tag{1}$$

Accordingly, the governing kinematic relations in the framework of the geometrically linear theory become

$$\varepsilon_{xx} = \partial_x u_x, \quad \varepsilon_{yy} = \partial_y u_y, \quad \varepsilon_{xy} = \varepsilon_{yx} = \frac{1}{2}(\partial_x u_y + \partial_y u_x), \tag{2}$$

$$\omega = \frac{1}{2}(\partial_x u_y - \partial_y u_x), \quad \kappa_{xz} = \partial_x \omega, \quad \kappa_{yz} = \partial_y \omega, \tag{3}$$

where ε_{pq} are the components of the usual strain tensor, $\omega_z \equiv \omega$ is the rotation, and $(\kappa_{xz}, \kappa_{yz})$ are the non-vanishing components of the curvature tensor (i.e. the gradient of rotation) expressed in dimensions of $[\text{length}]^{-1}$.

For a homogeneous centrosymmetric and isotropic constrained Cosserat material the constitutive equations furnish

$$\sigma_{xx} = (\lambda + 2\mu)\varepsilon_{xx} + \lambda\varepsilon_{yy}, \quad \sigma_{yy} = (\lambda + 2\mu)\varepsilon_{yy} + \lambda\varepsilon_{xx}, \quad \sigma_{xy} + \sigma_{yx} = 4\mu\varepsilon_{xy} \tag{4}$$

and

$$m_{xz} = 4\mu\ell^2\kappa_{xz}, \quad m_{yz} = 4\mu\ell^2\kappa_{yz}, \tag{5}$$

where $(\sigma_{xx}, \sigma_{xy}, \sigma_{yx}, \sigma_{yy})$ and (m_{xz}, m_{yz}) are the non-vanishing components of the (asymmetric) stress and couple-stress tensors, respectively. Moreover, (μ, λ) stand for the Lamé moduli, and ℓ is the characteristic material length of constrained

Cosserat theory [19]. The characteristic length ℓ is associated with the strain energy of a couple-stress medium.

In the absence of body forces and body moments, the equations of motion in terms of the displacement components (u_x, u_y) become [28]

$$\mu\nabla^2 u_x + (\lambda+\mu)\partial_x e - \mu\ell^2\nabla^2[\nabla^2 u_x - \partial_x e] = \rho\ddot{u}_x + 2\rho h^2\partial_y\ddot{\omega}, \tag{6}$$

$$\mu\nabla^2 u_y + (\lambda+\mu)\partial_y e - \mu\ell^2\nabla^2[\nabla^2 u_y - \partial_y e] = \rho\ddot{u}_y - 2\rho h^2\partial_x\ddot{\omega}, \tag{7}$$

where ∇^2 is the 2D Laplace operator and $e = \partial_x u_x + \partial_y u_y$ denotes the dilatation. In addition, ρ is the mass density and h is a characteristic intrinsic material length associated with the micro rotational inertia of the continuum. According to Mindlin [45], this length can be related to the size of the edges of the unit cells that the material is composed. The influence of microinertia on transient dynamic problems has been highlighted in [46] and [47]. Moreover, an interrelation of the two characteristic microstructural lengths ℓ and h was given by Georgiadis and Velgaki [44] by comparing the forms of dispersion curves of Rayleigh waves in couple-stress theory with the ones obtained by the discrete particle theory (atomic-lattice approach). Finally, we note that the superposed dot in Eqs (6) and (7) denotes time differentiation and that use of a Cartesian coordinate system centered at the crack-tip at time $t = 0$ is being made.

Although the above system is much more complicated than that in the respective case of classical elastodynamics, uncoupling by the use of Lamé-type potentials still proves to be successful. The potentials $\phi(x, y, t)$ and $\psi(x, y, t)$ are defined in terms of the displacement components as

$$u_x = \frac{\partial\phi}{\partial x} + \frac{\partial\psi}{\partial y}, \quad u_y = \frac{\partial\phi}{\partial y} - \frac{\partial\psi}{\partial x}. \tag{8}$$

Incorporating the above relations into (6) and (7), the following uncoupled PDEs are obtained which constitute our governing field equations. It turns out that the potential ϕ satisfies a second order PDE, whereas the potential ψ satisfies a PDE of the fourth order, i.e.

$$c_p^2\nabla^2\phi = \ddot{\phi}, \tag{9}$$

$$c_s^2\left(1 - \ell^2\nabla^2\right)\nabla^2\psi = \left(1 - h^2\nabla^2\right)\ddot{\psi}, \tag{10}$$

where $c_p = [(\lambda+2\mu)/\rho]^{1/2}$ and $c_s = (\mu/\rho)^{1/2}$ are the velocities of the pressure (P) and shear (S) waves, respectively, in the classical elasticity theory. The completeness of the representation (8) in dynamic couple-stress elasticity has be proven in [28].

It is interesting to note that Eq.(9) is related to the propagation of pressure waves and has the same form with the respective one in the classical theory. This, in turn, implies that pressure waves are not dispersive in the context of the constrained Cosserat elasticity and their phase velocity is the same as in

the classical theory, $v_p = c_p$ (see also [35]) . On the other hand, unlike the corresponding case of classical elastodynamics, Eq.(10) is of the fourth order which means that shear waves become dispersive. It is straightforward to show that the phase velocity v_s of the shear waves in a constrained Cosserat medium takes the following form

$$v_s = c_s(1 + \ell^2 s^2)^{1/2}(1 + h^2 s^2)^{-1/2}, \tag{11}$$

which shows that the propagation velocity depends upon the wavenumber s. Accordingly, the group velocity v_s^g at which the energy propagates in a dispersive medium becomes

$$v_s^g = v_s + (\ell^2 - h^2)c_s s^2(1 + \ell^2 s^2)^{-1/2}(1 + h^2 s^2)^{-3/2}. \tag{12}$$

The following three cases are then distinguished: (i) For $\ell < h$, Eq. (12) implies that $v_s^g < v_s$, thus the dispersion for shear waves is normal. (ii) For $\ell > h$, we have $v_s^g > v_s$ indicating that the dispersion is anomalous. (iii) For $\ell = h$ or $(\ell, h) \to 0$ (i.e. no material microstructure), the shear wave velocity degenerates into the non-dispersive velocity of classical elastodynamics.

A final comment pertains to the propagation of Rayleigh waves in a couple-stress medium. As it was shown in [28] (see also [44]), Rayleigh waves become dispersive when couple-stress effects are taken into account. In fact, the phase velocity v_R becomes strongly dependent upon the ratio: $h_0 = h/\ell$ between the two competing characteristic material lengths of the theory.

Figure 1 illustrates the variation of the normalized phase velocity v_R/c_s of the Rayleigh waves in couple-stress elasticity versus the normalized wavenumber $s\ell$ for three values of the Poisson's ratio ν. It is observed that for small wavenumbers (low frequencies) the phase velocity of the Rayleigh wave tends to the respective classical value c_R. Such a result is intuitively expected since long wavelengths do not "capture" the material microstructure (see also Fig. 2 on the right). As the wavenumber increases (high frequency) the phase velocity departs from the classical value exhibiting an increasing or decreasing trend that depends upon the microstructural ratio h_0. In particular, it is observed that for $h_0 < h_0^*$ the phase velocity of the Rayleigh wave increases significantly as compared to the classical value, whereas for $h > h_0^*$, the phase velocity decreases. The curve $h_0 = h_0^*$ with $h_0^* \equiv h_0^*(\nu) = c_s/c_R$ differs slightly from the classical elasticity solution which shows that in this case the Rayleigh waves are *almost* non-dispersive. Note that the constant h_0^* depends, according to its definition, only upon the Poisson's ratio. In particular, for a material with Poisson's ratio in the range $0 \leq \nu \leq 0.5$, the constant h_0^* varies between $1.046 \leq h_0^* \leq 1.144$. The dispersive character of the Rayleigh waves is more pronounced in the range $0 < s\ell < 3$. As the normalized wavenumber increases further, $s\ell > 3$, the phase velocity reaches a plateau attaining a constant value which depends on the Poisson's ratio ν and the ratio h_0. This implies, in turn, that when the wavelength Λ is less than 2ℓ (recall that $\Lambda = 2\pi/s$), the Rayleigh waves in couple-stress elasticity become again non-dispersive. It is worth noting that when $h > h_0^*$, the minimum velocity

becomes $v_R = c_s/h_0$ and is obtained in the limit as $s \to \infty$. Moreover, when the micro-inertia is zero, $h_0 = 0$, the speed of the Rayleigh waves in couple-stress elasticity is always greater than the corresponding one in the classical theory and reaches a maximum value as $s \to \infty$. This is contrast with the corresponding case of antiplane motions in a couple-stress elastic half-space where the speed of the surface waves increase monotonically without bound as $s \to \infty$ [29].

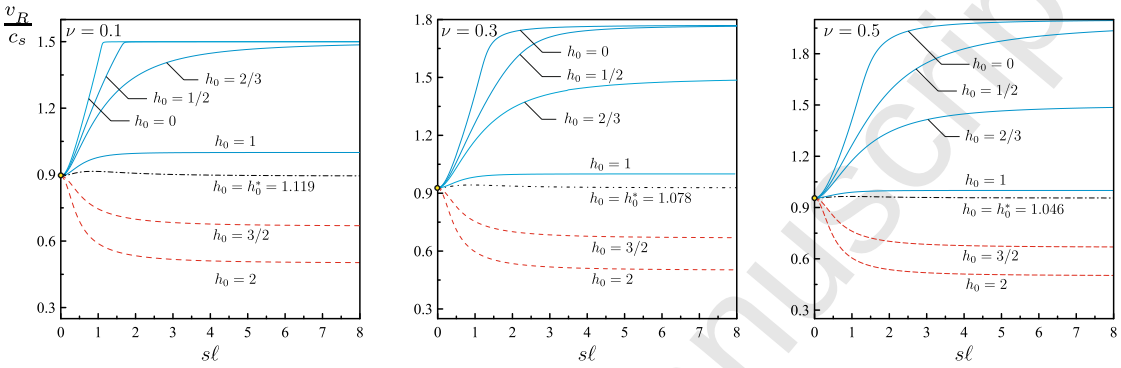

Figure 1: Variation of the normalized Rayleigh wave phase velocity v_R/c_s with respect to the normalized wavenumber $s\ell$ for various Poisson's ratios ν in couple-stress elasticity.

Further, Figure 2 shows the variation of the normalized group velocity v_R^g/c_s of Rayleigh waves for a material with Poisson's ratio $\nu = 0.3$ and $h_0^* = 1.078$ versus the normalized wavenumber (*left*) and the normalized wavelength Λ/ℓ (*right*). It is observed that the dispersion characteristics are controlled primarily by the ratio h_0. In particular, for $h_0 < h_0^*$, the group velocity becomes larger than the phase velocity showing that the dispersion is anomalous, a result which is in agreement with experiments in granular type materials such as ceramics, bones and cellular materials (see e.g.[48, 49, 50]). More specifically, an anomalous dispersion is observed in the range $2\ell < \Lambda < 12\ell$ and for decreasing ratios h_0. For $h_0 = 0$, the group velocity exhibits a peak around $s = \ell$ (or $\Lambda = 6\ell$, Fig. 2 on the right) which is attributed to the fact that the gradient of the phase velocity with respect to the wavenumber at the same point changes abruptly. This implies a strong anomalous dispersion where the wavelets of the carrier wave are building up at the front of the group. On the other hand, for $h_0 > h_0^*$, the group velocity decreases with respect to the phase velocity showing normal dispersion characteristics, a result which is in agreement with atomic lattice theories [43] and holds for most metals and alloys ([51, 52]). Moreover, normal dispersion characteristics are observed in guided seismic Rayleigh waves (Rg-waves) which are generated near ground surfaces due to seismic events such as rock or mine-bursts, industrial or underground nuclear explosions [53].

In light of the above discussion, a velocity V is characterized as sub-Rayleigh (for all wavenumbers) when $V < v_R$. Hence, for a steady-state motion, it suffices that the propagation velocity is less than the classical Rayleigh velocity i.e. $V < c_R$ when $0 \le h_0 \le h_0^*$, whereas for $h_0 > h_0^*$ the propagation is sub-Rayleigh provided that $V < c_s/h_0$. The conditions for sub-Rayleigh propagation are sum-

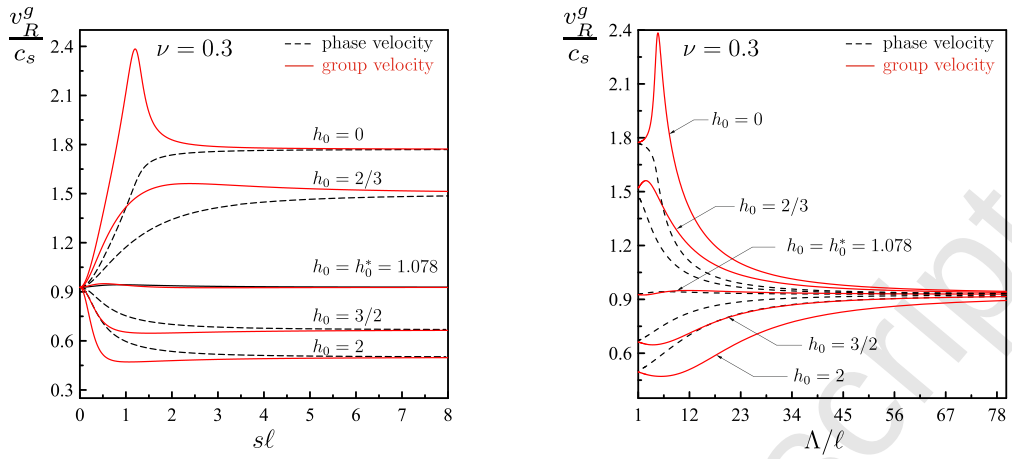

Figure 2: Variation of the normalized Rayleigh wave group velocity v_R^g/c_s with respect to the normalized wavenumber $s\ell$ (left) and the normalized wavelength Λ/ℓ (right) in couple-stress elasticity. The respective phase velocities are depicted also for comparison.

marized in the following inequalities:

$$\text{sub-Rayleigh velocity}: \quad \begin{cases} V < c_R, & \text{for} \quad 0 \le h_0 \le h_0^*, \\ V < c_s/h_0, & \text{for} \quad h_0 > h_0^*. \end{cases} \tag{13}$$

It is therefore apparent that in constrained Cosserat elasticity the limiting propagation velocity depends upon the material microstructure through the characteristic lengths h and ℓ. As the second inequality in (13) suggests, for a material with $h/\ell > h_0^*$, the limiting speed becomes less than the classical Rayleigh velocity. For example, when $\nu \in (0.2, 0.3)$ (typical for rock materials) and $1.2 < h/\ell < 1.5$, the limiting Rayleigh velocity ranges from $u_R = 0.6c_s \sim 0.7c_s$ which verifies experimental observations regarding the limiting propagation velocity in shear rupture of faults [7].

3. Steady state shear crack propagation

Consider now a semi-infinite crack in a body of infinite extent governed by the equations of plane strain couple-stress elasticity. The crack propagates with constant sub-Rayleigh velocity V along the x-axis and is subjected to a distribution of shear tractions $\tau(x)$ along the crack faces moving with the same velocity. The standard steady-state assumption for moving sources is adopted [54] and the new moving Cartesian coordinate system: $X = x - Vt$ and $Y = y$ is employed for the analysis. In this way, any transients can reasonably be avoided (therefore gaining considerable simplification in the analysis). In the moving framework, the field equations (9) and (10) for the Lamé potentials $\phi(X, Y)$ and $\psi(X, Y)$ can now be written as

$$(1 - m^2c^2)\frac{\partial^2\phi}{\partial X^2} + \frac{\partial^2\phi}{\partial Y^2} = 0, \tag{14}$$

$$(1-m^2)\frac{\partial^2\psi}{\partial X^2}+\frac{\partial^2\psi}{\partial Y^2}-\ell^2\left[\left(1-m^2h_0^2\right)\frac{\partial^2(\nabla^2\psi)}{\partial X^2}+\frac{\partial^2(\nabla^2\psi)}{\partial Y^2}\right]=0, \tag{15}$$

where $c=c_s/c_p=\left[(1-2\nu)/2(1-\nu)\right]^{1/2}<1$. Also, $m=V/c_s$ and $mc=V/c_p$ are the two Mach numbers. It is worth noting that $m<m_R$ with $m_R=\min\{1/h_0,1/h_0^*\}$ and $h_0^*=c_s/c_R$, in order for the crack to propagate with a sub-Rayleigh speed (see also Section 2). Figure 3 depicts the sub-Rayleigh and the super-Rayleigh regimes in couple-stress elasticity.

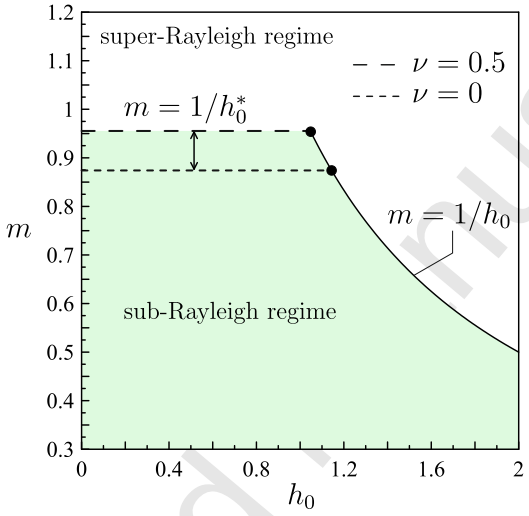

Figure 3: Sub-Rayleigh and Super-Rayleigh regimes in the $m-h_0$ plane.

Moreover, in view of Eqs (4)-(7), the stresses and couple-stresses assume the following form in the steady state case

$$\begin{aligned}
\sigma_{xx}&=\lambda\nabla^2\phi+2\mu\left(\frac{\partial^2\phi}{\partial X^2}+\frac{\partial^2\psi}{\partial X\partial Y}\right),\\
\sigma_{yy}&=\lambda\nabla^2\phi+2\mu\left(\frac{\partial^2\phi}{\partial Y^2}-\frac{\partial^2\psi}{\partial X\partial Y}\right),\\
\sigma_{yx}&=\mu\left[2\frac{\partial^2\phi}{\partial X\partial Y}+\frac{\partial^2\psi}{\partial Y^2}-\frac{\partial^2\psi}{\partial X^2}\right]-\mu\ell^2\nabla^4\psi+\mu m^2h^2\nabla^2\psi,\\
\sigma_{xy}&=\mu\left[2\frac{\partial^2\phi}{\partial X\partial Y}+\frac{\partial^2\psi}{\partial Y^2}-\frac{\partial^2\psi}{\partial X^2}\right]+\mu\ell^2\nabla^4\psi-\mu m^2h^2\nabla^2\psi,
\end{aligned} \tag{16}$$

$$m_{xz}=-2\mu\ell^2\frac{\partial(\nabla^2\psi)}{\partial X},\quad m_{yz}=-2\mu\ell^2\frac{\partial(\nabla^2\psi)}{\partial Y}. \tag{17}$$

Due to the anti-symmetry with respect to the $Y=0$ plane, the problem can be viewed as a half-plane problem in the region $Y\geq 0$ under the following boundary

conditions

$$\sigma_{yx}(X, Y=0) = -\tau(X) \qquad \text{for} \qquad -\infty < X < 0, \tag{18}$$

$$\sigma_{yy}(X, Y=0) = 0 \qquad \text{for} \qquad -\infty < X < \infty, \tag{19}$$

$$m_{yz}(X, Y=0) = 0 \qquad \text{for} \qquad -\infty < X < \infty, \tag{20}$$

$$u_x(X, Y=0) = 0 \qquad \text{for} \qquad 0 < X < \infty, \tag{21}$$

where the distribution of shear tractions along the crack faces which is assumed to have the following form [29]

$$\tau(X) = \frac{(-1)^p}{\Gamma(1+p)} \frac{T_0}{L} \left(\frac{X}{L}\right)^p \mathrm{e}^{X/L}, \quad X < 0, \quad p = 0, 1, 2, 3... \tag{22}$$

where $\Gamma()$ is the Gamma function, p is a positive integer, and T_0 and L are positive constants having pertinent dimensions. The distribution of the shear traction along the crack faces is depicted in Fig.4 for various values of the loading parameter p and $L/\ell = 10$. It is noted that maximum of the distributed traction occurs at $X_{max} = -pL$, whereas the resultant force due to the applied traction on the crack faces is: $\int_{-\infty}^{0} \tau(X) dX = T_0$ and is applied at a distance: $(1/T_0) \int_{-\infty}^{0} \tau(X) X dX = -(1+p)L$. Note further that for $p = 0$ the load at the crack-tip ($X = 0$) attains its maximum value, while for $p > 0$ it becomes null at the crack-tip. Moreover, as the parameter p decreases the maximum value of the traction increases and the distribution becomes more localized near the crack-tip.

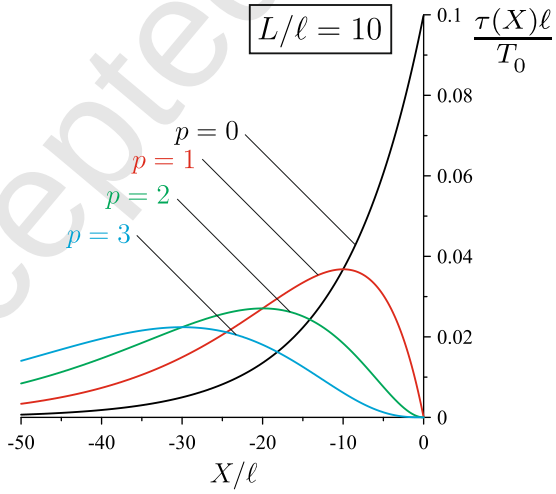

Figure 4: Variation of the normalized shear traction $\tau(X)\ell/T_0$ applied along the crack faces versus the normalized distance X/ℓ for various loading parameters p.

4. Full field solution

An exact solution of the shear crack problem is obtained by means of the Fourier transform and the Wiener-Hopf technique. The basic transform analysis and the

general factorization procedure was thoroughly illustrated in [28]. The unilateral Fourier transforms of the unknown stress $\sigma_{yx}(X>0, Y=0)$ ahead of the crack tip, and the unknown crack-face displacement $u_x(X<0, Y=0)$ are defined as follows

$$\Sigma^+(s) = \int_0^\infty \sigma_{yx}(X, Y=0) e^{isX}\, dX, \quad U^-(s) = \int_{-\infty}^0 u_x(X, Y=0) e^{isX}\, dX. \tag{23}$$

The transformed function $\Sigma^+(s)$ is analytic in the upper half-plane $\mathrm{Im}(s) > 0$, while $U^-(s)$ is analytic in the lower half-plane $\mathrm{Im}(s) < 0$. The latter definitions in conjunction with the boundary conditions (18)-(21) provide the final Wiener-Hopf equation of the problem, connecting the two unknown functions $\Sigma^+(s)$ and $U^-(s)$ [28]

$$\Sigma^+(s) - T^-(s) = \frac{\mu\ell(1-\phi)(2-m^2)^2\, s^2}{m^2\left[(s\ell)^2\right]^{1/2}} N(s\ell) U^-(s), \tag{24}$$

where $\phi \equiv \phi(m,\nu) = 4\left(1-m^2c^2\right)^{1/2}\left(2-m^2\right)^{-2}$ and $T^-(s)$ is the unilateral Fourier transform of the shear loading along the crack-faces which according to Eq. (22) is given as

$$T^-(s) = \frac{T_0}{(1+isL)^{1+p}}. \tag{25}$$

The kernel function $N(z)$ is defined as

$$N(z) = \frac{\theta(z)^2 + \left[z^2\right]^{1/2}\theta(z) + m^2}{\ell(1-\phi)\left[\beta(z)+\gamma(z)\right]\theta(z)} - \frac{\phi}{1-\phi}, \tag{26}$$

where

$$\theta(z) = \ell^2\, \frac{\beta(z)\gamma(z)}{\left[z^2\right]^{1/2}}, \tag{27}$$

and

$$\beta(z) = \frac{\left[1 + \left(2-m^2h_0^2\right)z^2 + \chi(z)\right]^{1/2}}{\sqrt{2}\ell}, \quad \gamma(z) = \frac{\left[1 + \left(2-m^2h_0^2\right)z^2 - \chi(z)\right]^{1/2}}{\sqrt{2}\ell}, \tag{28}$$

$$\chi(z) = \left[1 + 2\left(2-h_0^2\right)m^2z^2 + m^4h_0^4z^4\right]^{1/2}, \tag{29}$$

with $z = s\ell$ being a dimensionless complex variable.

The kernel function possesses the desired asymptotic property $\lim_{|z|\to\infty} N(z) = 1$ and has no poles or zeros in the finite complex z-plane. It can be further shown that the branch cuts of the kernel function $N(z)$ extend along: $\pm\varepsilon \le \mathrm{Im}(z) \le \pm b_0$, and $\pm b_0 \le \mathrm{Im}(z) \le \pm b_1$, with ε being a real number such that $\varepsilon \to 0$ and

$$b_0 = \frac{\left(1-m^2\right)^{1/2}}{\left(1-m^2h_0^2\right)^{1/2}}, \quad b_1 = \frac{\left(2-h_0^2-2\left(1-h_0^2\right)^{1/2}\right)^{1/2}}{mh_0^2}. \tag{30}$$

Note that in the sub-Rayleigh regime ($m < m_R$) the constant b_0 is always real, while the constant b_1 is real when $h_0 \leq 1$ and complex for $h_0 > 1$. As it was shown in [28], the kernel is factorized as: $N(z) = N^+(z)N^-(z)$ where the sectionally analytic functions $N^{\pm}(z)$ read

$$N^{\pm}(z) = \exp\left\{-\frac{1}{\pi}\left[\int_0^{ib_0} \tan^{-1}\left[\frac{\mathrm{Im}\left(N(\zeta)\right)}{\mathrm{Re}\left(N(\zeta)\right)}\right]\frac{d\zeta}{\zeta \pm z} + \mathfrak{a}\int_{ib_0}^{ib_1} \tan^{-1}\left[\frac{\mathrm{Im}\left(N(\zeta)\right)}{\mathrm{Re}\left(N(\zeta)\right)}\right]\frac{d\zeta}{\zeta \pm z}\right]\right\}, \tag{31}$$

with $\mathfrak{a}$ being a constant that takes the values 0 or 1 depending on the branches of the kernel function $N(z)$ defined as

$$\mathfrak{a} = \begin{cases} 1 - \mathcal{H}\left(\sqrt{1-\sqrt{1-h_0^2}} - mh_0\right), & \text{for } h_0 \leq 1 \\ 0, & \text{for } h_0 > 1 \end{cases} \tag{32}$$

where $\mathcal{H}(\ )$ is the Heaviside step function. This implies that the second branch of $N(z)$ exists only in certain cases, depending on the values of (m, h_0).

The Wiener-Hopf equation (24) can then be conveniently written in the form:

$$\frac{\Sigma^+(s)\,[s\ell]_+^{1/2}}{N^+(s\ell)} = \frac{\mu\ell(1-\phi)\left(2-m^2\right)^2 s^2}{m^2\,[s\ell]_-^{1/2}} N^-(s\ell)U^-(s) + T_0 M(s\ell), \tag{33}$$

where the functions $[s\ell]_+^{1/2}$ and $[s\ell]_-^{1/2}$ are analytic in the upper and lower half plane [28], respectively and

$$M(z) = \frac{(-z_0)^{p+1}\,[z]_+^{1/2}}{(z-z_0)^{p+1}N^+(z)}, \tag{34}$$

with $z_0 = i\ell/L$.

The sum-splitting of the last term in the RHS of Eq. (33) is required to complete the decoupling process. This is done by exploiting the fact that the function $[z]_+^{1/2}/N^+(z)$ is analytic at z_0, and, thus, admits a Taylor series representation. In particular, we obtain

$$\frac{(-z_0)^{p+1}\,[z]_+^{1/2}}{N^+(z)} = (-z_0)^{p+1}\sum_{j=0}^{p} c_j(z-z_0)^j + M^+(z)(z-z_0)^{p+1}. \tag{35}$$

In view of the above, $M(z)$ can be factorized as

$$M(z) = M^+(z) + M^-(z), \tag{36}$$

where $M^+(z)$ is defined by Eq. (35) and is analytic in the upper half-plane, while $M^-(z)$ is defined as

$$M^-(z) = (-z_0)^{p+1}\sum_{j=0}^{p} c_j(z-z_0)^{j-p-1}, \tag{37}$$

and is analytic in the half-plane $\mathrm{Im}(z) < \ell/L$. It is further remarked that the functions $M^+(z)$ and $M^-(z)$ exhibit the following asymptotic behavior: $M^{\pm}(z) = O(1)$ as $|z| \to 0$ and $M^{\pm}(z) = O(z^{-1})$ as $|z| \to \infty$.

The constants c_j can be formally derived as

$$c_j = \frac{1}{2\pi i} \oint_C \frac{[z]_+^{1/2}}{N^+(z)(z-z_0)^{j+1}} dz, \tag{38}$$

where C is an arbitrary contour centered at the point $z = z_0$ and lying in the analyticity domain. Substituting Eq. (36) into (33), we finally derive

$$\begin{aligned} \frac{\Sigma^+(s)\ [s\ell]_+^{1/2}}{N^+(s\ell)} - T_0 M^+(s\ell) = & \frac{\mu\ell(1-\phi)\,(2-m^2)^2\ s^2 N^-(s\ell)}{m^2\,[s\ell]_-^{1/2}} U^-(s) \\ & + T_0 M^-(s\ell) \equiv E(s\ell). \end{aligned} \tag{39}$$

The above functional equation defines the function $E(s\ell)$ only on the real line. In view of the results obtained in [28], the functions $\Sigma^+(s)$ and $U^-(s)$ exhibit the following asymptotic behavior as $|s| \to \infty$: $\Sigma^+(s) = O(s^{-1/2})$ $(\mathrm{Im}(s) > 0)$ and $U^-(s) = O(s^{-3/2})$ $(\mathrm{Im}(s) < 0)$. Moreover, bearing in mind that: $N^{\pm}(s\ell) \to 1$ and $M^{\pm}(s\ell) \to 0$ as $|s| \to +\infty$, we conclude that the both members of (39) tend to a constant value at infinity, which according to Liouville's theorem implies, in turn, that $E(s\ell) = T_0 E_0$, where E_0 is a constant.

The transformed shear stress is now given by (39) as

$$\Sigma^+(s) = T_0[E_0 + M^+(s\ell)]\, N^+(s\ell)\, [s\ell]_+^{-1/2}, \tag{40}$$

which is analytic for $\mathrm{Im}(s) > 0$.

The constant E_0 can be determined from simple equilibrium considerations. In particular, taking into account that $\Sigma^+(0) = \int_0^\infty \sigma_{yx}(X, Y = 0)\, dX = T_0$, it can readily be shown that

$$E_0 = -M^+(0) = \sum_{j=0}^{p} c_j (-i\ell/L)^j. \tag{41}$$

Note that alternatively, the constant E_0 can be evaluated from the condition $u_x(0,0) = 0$ which is equivalent to $\int_{-\infty}^{+\infty} U^-(s) ds = 0$.

The final transformed expression for the crack-face displacement becomes then

$$U^-(s) = \frac{T_0 m^2}{\mu\ell(1-\phi)\,(2-m^2)^2} \left[E_0 - M^-(s\ell)\right] \frac{[s\ell]_-^{1/2}}{s^2 N^-(s\ell)}, \tag{42}$$

which is analytic for $\mathrm{Im}(s) < 0$.

Accordingly, using asymptotic analysis, the following near-tip field behavior is obtained for the shear stress ahead of the crack-tip and the crack-face displacement

$$\sigma_{yx}(X \to +0, Y = 0) = \frac{\sqrt{2} T_0\, \mathrm{Re}(E_0)}{\sqrt{\pi\ell}}\, X^{-1/2}, \quad X > 0, \tag{43}$$

$$u_x(X \to -0, Y = 0) = \frac{2\sqrt{2}T_0\, m^2\, \mathrm{Re}(E_0)}{\mu\sqrt{\pi\ell}(\phi - 1)\,(2 - m^2)^2}\,(-X)^{1/2}, \quad X < 0. \tag{44}$$

The dynamic (d) stress intensity factor (SIF) assumes then the following form

$$K_{\mathrm{II}}^{d} = \lim_{X\to 0}\sqrt{2\pi X}\sigma_{yx}(X, Y = 0) = 2\,T_0\frac{\mathrm{Re}\,(E_0)}{\sqrt{\ell}}, \tag{45}$$

whereas the classical (cl.) SIF $K_{\mathrm{II}}^{d_{cl.}}$ reads (an analytical derivation is shown in Appendix A)

$$K_{\mathrm{II}}^{d_{cl.}} = \frac{T_0\sqrt{2}\Gamma(1/2 + p)}{\sqrt{\pi L}\,\Gamma(1 + p)}, \tag{46}$$

with $\Gamma()$ being the Gamma function. It is interesting to note that the classical SIF does *not* depend upon the crack speed V. This is a common feature of steady-state crack propagation problems in the classical elastodynamic theory [54] (see also [29], Appendix A) and is in marked contrast with the present finding where the dynamic SIF in (45) depends upon the speed of the propagation through the Liouville's constant E_0 for all loading profiles.

5. Results and discussion

5.1. Analytical representation of displacements, stresses and couple-stresses

The exact behavior of the shear stress ahead of the crack tip and the crack opening displacement can be obtained from (40) and (42), respectively, by employing the inverse Fourier transform. In particular, for a crack propagating with a sub-Rayleigh speed, the functions $\Sigma^+(s)$ and $U^-(s)$ have no branch points or poles along the real line, consequently, the path of integration $\mathcal{L}$ coincides with the real line in the complex s-plane

$$\sigma_{yx}(X) = \frac{1}{2\pi}\int_{-\infty}^{\infty}\Sigma^+(s)e^{-iXs}ds, \qquad X > 0. \tag{47}$$

$$u_x(X) = \frac{1}{2\pi}\int_{-\infty}^{\infty}U^-(s)e^{-iXs}ds, \qquad X < 0, \tag{48}$$

The variation of the normalized sliding crack-face displacement $\mu u_x/T_0$ is depicted in Figure 5 with respect to the normalized distance X/ℓ and a range of values of the loading parameter $p = \{0, 1, 2\}$. The Poisson's ratio is $\nu = 0.3$, $L/\ell = 10$ and $h_0^* = 1.078$. Two cases regarding the effect of the microstructural ratio h_0 are examined: (i) $h_0 = 0$ (zero micro-inertia), characterized by anomalous dispersion of Rayleigh waves and a limiting crack propagation velocity: $V = c_R = 0.927c_s$ - (Fig.5, *upper row*), and (ii) $h_0 = 1.1h_0^*$, characterized by normal dispersion of Rayleigh waves and a limiting crack propagation velocity: $V = c_s/h_0 = 0.843c_s$ - (Fig.5, *lower row*). It is observed that in all cases the

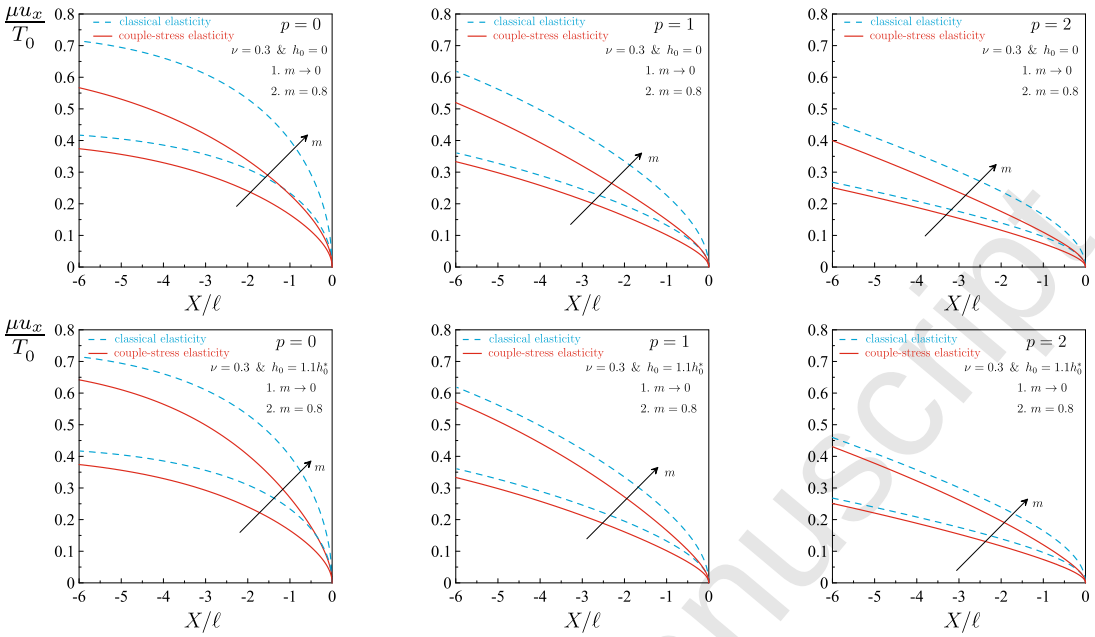

Figure 5: Variation of the normalized upper crack face sliding displacement versus the normalized distance for three different values of the loading parameter $p = \{0, 1, 2\}$. **(upper row)** $h_0 = 0$ - zero microinertia **(lower row)** $h_0 = 1.1h_0^*$. The Poisson's ratio is $\nu = 0.3$, $L/\ell = 10$, and $h_0^* = 1.078$.

sliding crack-face displacement in couple-stress elasticity (red solid line) is smaller than the one predicted by the classical LEFM theory (blue dashed line) verifying that the microstructure can shield the crack-tip from fracture. This shielding effect becomes more pronounced as the ratio L/ℓ decreases i.e. when the microstructure of the material is comparable with the geometrical characteristics of the problem. The same trend was observed also in the static case (Gourgiotis et al. [55]). As the crack propagation velocity approaches the pertinent Rayleigh limit $m \to m_R$, the sliding displacement increases significantly but contrary to the classical case it remains finite in magnitude. The micro-inertia does not affect much the variation of the displacement as it can be deduced by comparing the upper row with the lower row in Figure 5. Indeed, higher values of the ratio h_0 result to only a small increase in the sliding displacement which becomes more pronounced when the propagation velocity tends to the Rayleigh limit.

On the other hand, the loading profile plays an important role in the macroscopic response of the material. As Figure 6 illustrates, in all cases, the sliding displacement increases as we move along the crack-faces reaching a bounded maximum and then decreases monotonically to zero. An increase in the magnitude of u_x is noted for smaller values of the parameter p in a region close to the crack-tip (see also Fig. 5). However this trend is reversed as as we move away from the crack-tip and the sliding displacement becomes higher for greater values of the parameter p. In fact, it is observed that the maximum value of the sliding displacement increases for increasing p and its location is translated to the left.

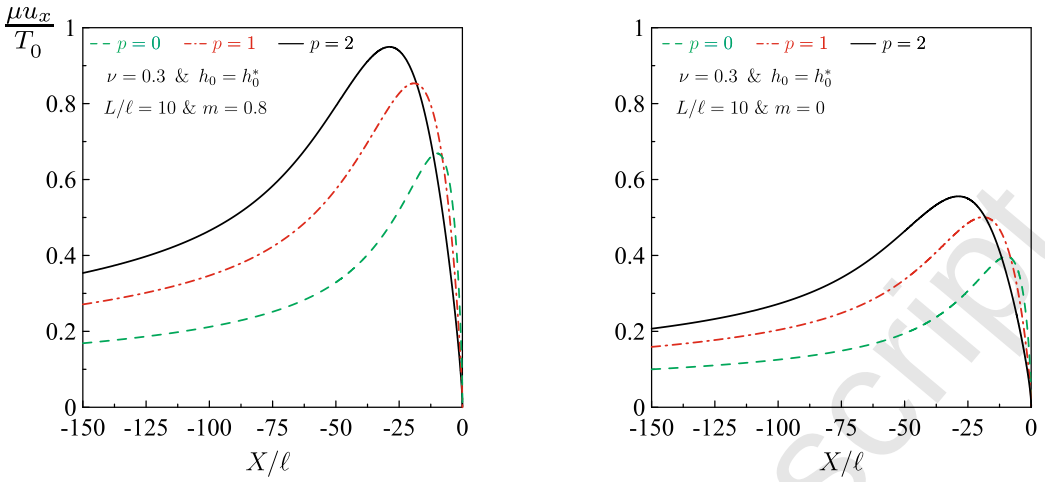

Figure 6: Effect of the loading parameter p on the variation of the normalized upper crack face sliding displacement in the dynamic case - $m=0.8$ (**left**) and static case - $m=0$ (**right**). The Poisson's ratio is $\nu=0.3$, $L/\ell=10$, and $h_0^*=1.078$.

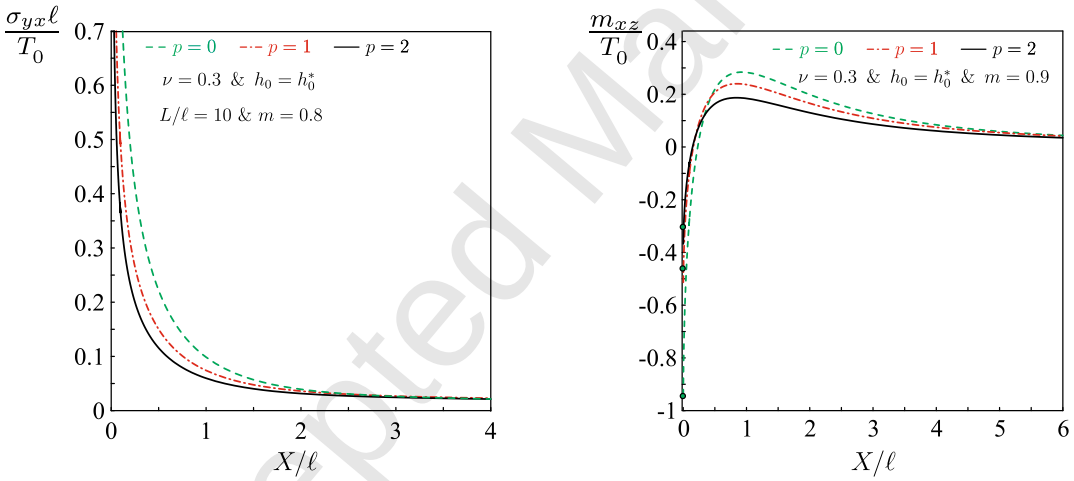

Figure 7: Effect of the loading parameter p on the variation of (**left**) the normalized shear stress and (**right**) the normalized couple-stress ahead of the crack-tip. The Poisson's ratio is $\nu=0.3$, $L/\ell=10$, and $h_0^*=1.078$.

Finally, Figure 7 on the left depicts the variation of the normalized shear stress $\sigma_{yx}\ell/T_0$ ahead of the crack-tip for three values of the loading parameter p. The propagation velocity of the crack is $V=0.8c_s$ and $h_0=h_0^*$. In this case, the limiting velocity is the classical Rayleigh speed $V=0.927c_s$. As in the classical theory, the shear stress remains square-root singular at the crack-tip. A stress aggravation is observed for lower values of p. Figure 7 on the right shows the effect of the loading parameter p on the variation of the normalized couple-stress m_{xz}/T_0 ahead of the crack-tip. It is observed that the couple-stress decays rapidly with increasing distance from the tip of the crack. Moreover, it is remarked that as in the static case [55], m_{xz} is bounded at the crack-tip.

5.2. The dynamic stress intensity factor

In this Section, we examine the dependence of the dynamic SIF $K_{\rm II}^d$ upon the crack speed, the loading profile, and the microstructural lengths of constrained Cosserat elasticity. It is recalled (see Section 4), that the *classical* dynamic SIF, Eq. (46), is independent of the propagation velocity and thus coincides with the static one: $K_{\rm II}^{d_{cl.}} = K_{\rm II}^{s_{cl.}}$.

Figure 8 depicts the variation of the ratio $K_{\rm II}^d/K_{\rm II}^s$ with respect to the normalized speed m of the crack. $K_{\rm II}^s$ is the static SIF in couple-stress elasticity obtained as $m \to 0$ (see also [28], [55]). Three different loading profiles are examined, namely, $p = \{0, 1, 2\}$. Note that when $h_0 \leq h_0^*$, the limiting velocity for sub-Rayleigh motion is $m = 1/h_0^*$ (i.e. $V = c_R$), while for $h_0 > h_0^*$ the limiting velocity is $m = 1/h_0$ (i.e. $V = c_s/h_0$). In particular, for a material with $\nu = 0.3$ we derive $h_0^* = 1.078$ and thus when $h_0 = 1.1h_0^*$ the limiting Rayleigh velocity becomes $0.84c_s$ showing a 9% decrease as compared to the classical limiting Rayleigh velocity. This finding shows that the limiting velocity of shear cracks can be lower for microstructured materials than the one predicted by the classical elastodynamic theory and is in agreement with experimental observations regarding the limiting propagation velocity of shear faults [7]. It is further noted that as the crack speed approaches the pertinent limiting velocity a significant but *finite* increase of the ratio $K_{\rm II}^d/K_{\rm II}^s$ is observed. This increase is more pronounced as $h_0 \to h_0^*$ (curve 2) and for higher values of the loading parameter p.

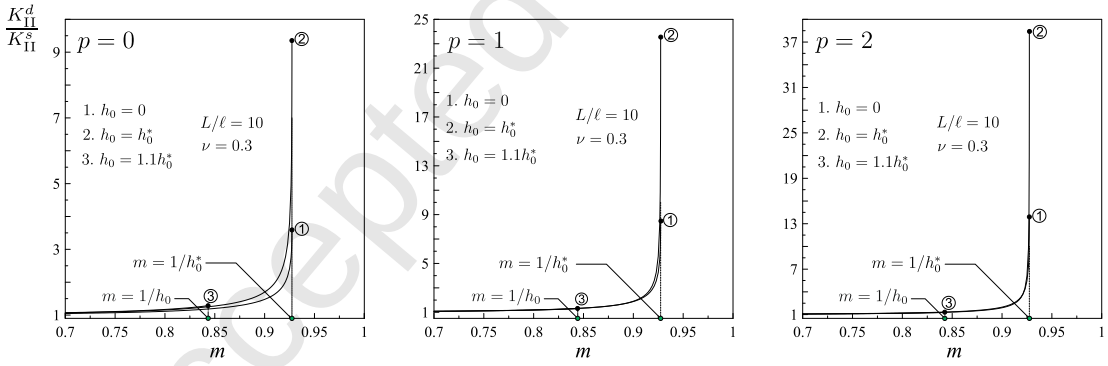

Figure 8: Variation of the ratio of the dynamic SIF to the static SIF in couple-stress elasticity with respect to the normalized crack speed m for $p = \{0, 1, 2\}$. The Poisson's ratio is $\nu = 0.3$ and $h_0^* = 1.078$.

Figure 9 illustrates the effect of the scale ratio L/ℓ upon the ratio of the dynamic SIFs in couple-stress and classical elasticity $K_{\rm II}^d/K_{\rm II}^{d_{cl.}}$. It is observed that in all cases the ratio is above unity. This shows a stress aggravation when couple-stress effects are taken into account. Moreover, the variation of the ratio depends strongly upon the loading profile. For $p = 0$, the ratio is a monotonically decreasing function of ℓ/L, while for $p > 0$ the ratio initially increases reaching a bounded maximum and then decreases monotonically. In the limit case $\ell/L \to 0$ the ratio of the SIFs in couple-stress and in classical theory is not unity but exhibits an increase which becomes more pronounced as the crack-tip velocity

approaches the limiting velocity (see also [28]). This limit value depends only upon the Poisson's ratio ν and the speed of the crack and is independent of the loading parameter p and the microstructural ratio h_0. When $m \to 0$ the limiting value becomes: $\sqrt{3-2\nu}$, recovering the result derived previously by Gourgiotis et al. (2012) in the static case. As Sternberg and Muki [56] pointed out the aggravation of the SIF can be attributed to the severe boundary layer effects of couple-stress elasticity in singular stress-concentration problems.

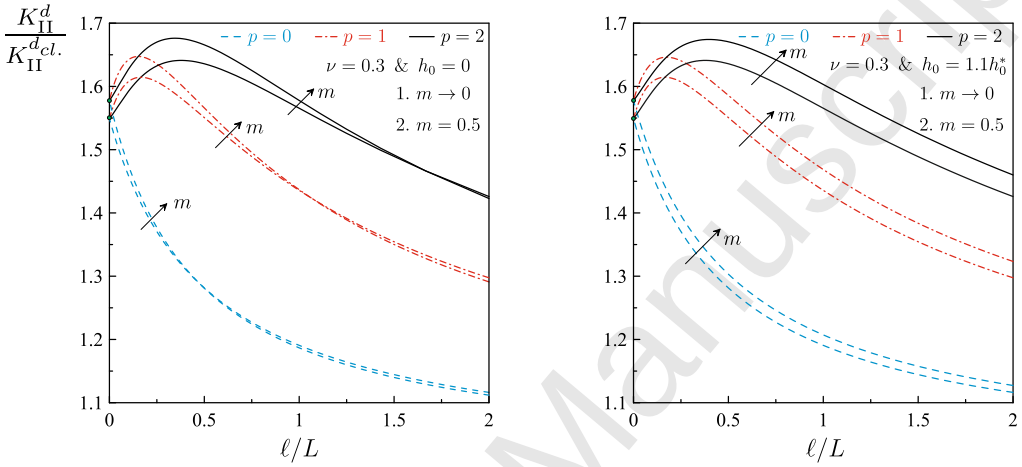

Figure 9: Variation of the ratio of the dynamic SIFs in couple-stress and classical elasticity with respect to L/ℓ for $h_0 = \{0, 1.1h_0^*\}$. The Poisson's ratio is $\nu = 0.3$ and $h_0^* = 1.078$.

5.3. The dynamic energy release rate

The dynamic J-integral was established in the context of couple-stress elasticity by Gourgiotis and Piccolroaz [28]. In the steady state case, the J-integral is identified as the energy release rate (ERR) and is path-independent [28]. For the evaluation of the ERR, we consider a rectangular shaped contour, centered at the crack-tip, with vanishing 'height' along the Y-direction and length 2ε. Letting $\varepsilon \to 0$, the contribution of the shear traction $\tau(X)$ along the crack faces vanishes allowing the use only of the asymptotic near-tip fields. For the plane-strain case considered here, the J-integral assumes the following form

$$J^d = -2\lim_{\varepsilon\to+0}\int_{-\varepsilon}^{\varepsilon}\left\{\sigma_{yy}(X,+0)\cdot\frac{\partial u_y(X,+0)}{\partial X}+\sigma_{yx}(X,+0)\cdot\frac{\partial u_x(X,+0)}{\partial X}\right.$$
$$\left.+\,m_{yz}(X,+0)\cdot\frac{\partial \omega(X,+0)}{\partial X}\right\}dX, \qquad (49)$$
$$= -2\lim_{\varepsilon\to+0}\int_{-\varepsilon}^{\varepsilon}\sigma_{yx}(X,+0)\cdot\frac{\partial u_x(X,+0)}{\partial X}dX$$

where we have used the fact that the normal stress $\sigma_{yy}(X,\pm 0)$ and the couple-stress $m_{yz}(X,\pm 0)$ are *zero* along the whole crack line ($Y=0$) in the mode II case.

Now, by utilizing the asymptotic solutions (43) and (44) and Fisher's theorem for products of singular distributions (see e.g. [57, 55, 28]), we finally obtain

$$J^d = \frac{2T_0^2 m^2 [\mathrm{Re}(E_0)]^2}{\mu\ell(\phi-1)\left(2-m^2\right)^2}, \tag{50}$$

On the other hand, the respective J-integral in the classical theory of elasticity is (Appendix A)

$$J^d_{cl.} = \frac{T_0^2 m^2 \sqrt{1-m^2}\,\Gamma(1/2+p)^2}{\mu\pi L\, R(m)\,\Gamma(1+p)^2} \tag{51}$$

where $R(m) = 4\left(1-m^2\right)^{1/2}\left(1-m^2c^2\right)^{1/2} - \left(2-m^2\right)^2$ is the classical Rayleigh function [54]. The roots of this function provide the Rayleigh wave speed in a classical non polar medium. As the speed of the crack reaches the *classical* Rayleigh wave velocity (i.e. $m \to c_R/c_s$) the Rayleigh function becomes zero and, consequently, the classical ERR in (51) becomes infinite. This is a common feature of steady-state problems in classical elasticity where the SIF does not depend upon the crack-tip velocity. On the other hand, for $\ell \neq 0$ (i.e. when couple-stress effects are taken into account) the ERR in (50) remains always *finite* in the range $m \in [0, m_R]$. Note further that as $\ell/L \to 0$, the ratio of the ERRs tends to unity

$$\lim_{\ell/L\to 0} \frac{J^d}{J^d_{cl.}} = 1. \tag{52}$$

Figure 10 illustrates the variation of the normalized ERR in couple-stress elasticity and in classical elasticity with respect to the normalized crack propagation velocity m for a material with $L/\ell = 10$ and $\nu = 0.3$. Three different loading profiles are examined: $p = \{0, 1, 2\}$. For curves 1 and 2 the limiting (sub-Rayleigh) velocity is $m_R = c_R/c_s = 1/h_0^* = 0.927$ with $h_0^* = 1.078$, whereas for curve 3 ($h_0 = 1.05h_0^*$) we have: $m_R = 1/h_0 = 0.883$. This justifies the fact the curve 3 terminates earlier than curves 1 and 2. As the speed approaches the respective limiting crack propagation velocity, an increase is observed in the dynamic ERR in couple-stress elasticity, however, contrary to the classical elasticity case (red dashed curve), the ERR remains always bounded. The increase becomes more significant when $h_0 = h_0^*$ (curve 2). This is attributed to the fact that in this case the Rayleigh waves travel *almost* non-dispersively in a couple-stress medium, thus, resembling the classical elasticity situation (see Fig. 1 and the relevant discussion in Section 3). Finally, it is noted that as the loading parameter increases the maximum values of the ERR in couple-stress elasticity increase accordingly. Comparing the graphs in Fig.10, we observe that the effect of the micro-inertia upon the ERR is more significant for lower values of the loading parameter p.

Figure 11 depicts the variation of the ratio of the ERR in couple-stress elasticity to the respective one in the classical LEFM theory versus the normalized

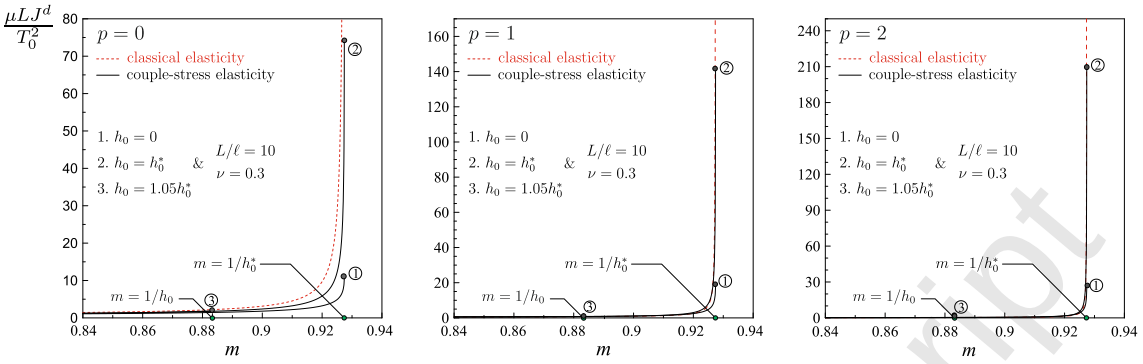

Figure 10: Distribution of the dynamic ERRs in couple-stress and classical elasticity with respect to the normalized crack speed for three different loading profiles $p = \{0, 1, 2\}$ and $h_0 = \{0, h_0^*, 1.05h_0^*\}$. The Poisson's ratio is $\nu = 0.3$, $L/\ell = 10$, and $h_0^* = 1.078$.

velocity for the cases: $h_0 \leq h_0^*$ (left) and $h_0 > h_0^*$ (right), respectively. Three different values of the loading parameter p are examined. It is observed that for $h_0 \leq h_0^*$ and $p = 0$, the ratio of the ERRs is below unity and exhibits a monotonically decreasing behavior with the crack speed. On the other hand, for $p > 0$ the ratio rises above unity showing an initial increase with increasing speed and then falling abruptly to zero as the crack reaches the Rayleigh velocity. This behavior is attributed to the fact that at the Rayleigh velocity limit the classical ERR becomes infinite and, accordingly, the ratio becomes zero (since the ERR in couple-stress elasticity remains always finite). A similar behavior was also observed in the case of a shear crack propagating with a sub-Rayleigh speed in a plane triangular-cell lattice ([58], [59]). The plane triangular-cell lattice consists of point particles which are connected by massless elastic bonds, thus, interacting only with forces and not internal moments. Such a model corresponds to the case of zero micro-rotational inertia ($h_0 = 0$) in the present study. Moreover, in the latter studies, the global ERR for the crack propagating through the homogenized medium can be identified with the classical ERR (Eq. (51) in our study), whereas the local ERR for the crack propagating through the lattice (i.e. the energy spent on fracture itself) corresponds to the ERR in couple-stress elasticity (Eq. (50) in our study). In the case $h_0 > h_0^*$, the pertinent Rayleigh limiting speed is defined as $m_R = 1/h_0$, which is evidently less than the classical Rayleigh velocity ($1/h_0^*$). Therefore, the curves plotted in Figure 11b terminate before they reach the zero value.

Finally, Figure 12 displays the dependence of the ratio $J^d/J^d_{cl.}$ upon the ratio of lengths ℓ/L. Depending on the loading profile a different behavior of the ratio is observed. In particular, for $p = 0$, the ratio $J^d/J^d_{cl.}$ decreases monotonically with increasing values of ℓ/L, remaining always *below* unity, $J^d/J^d_{cl.} < 1$. This decrease is more significant as the propagation speed approaches the Rayleigh limit velocity m_R. This finding shows that the couple-stress theory predicts a *strengthening* effect since a reduction of the crack driving force takes place as the material microstructure becomes more pronounced. Such strengthening effect has

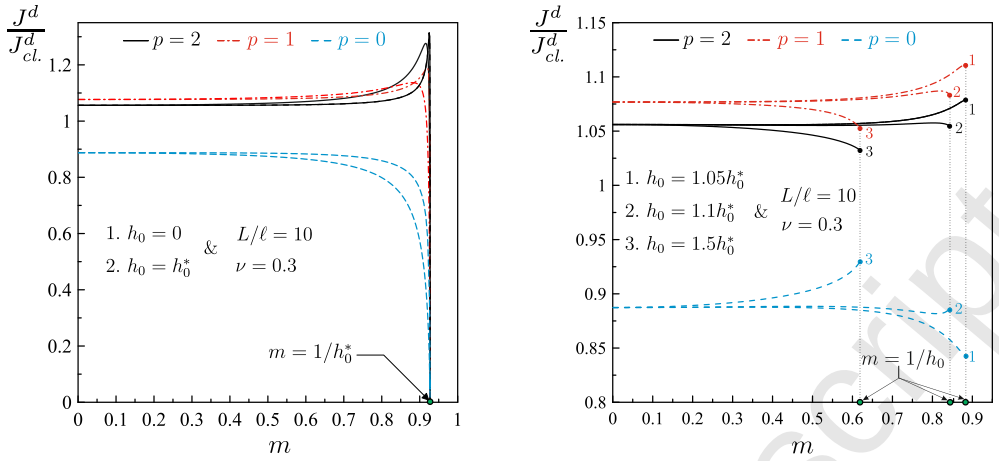

Figure 11: Variation of the ratio of the dynamic ERR in couple-stress elasticity to the ERR in classical elasticity with respect the normalized crack-tip velocity (**left**) for $h_0 \leq h_0^*$ and (**right**) for $h_0 > h_0^*$. The Poisson's ratio is $\nu = 0.3$, $L/\ell = 10$, and $h_0^* = 1.078$.

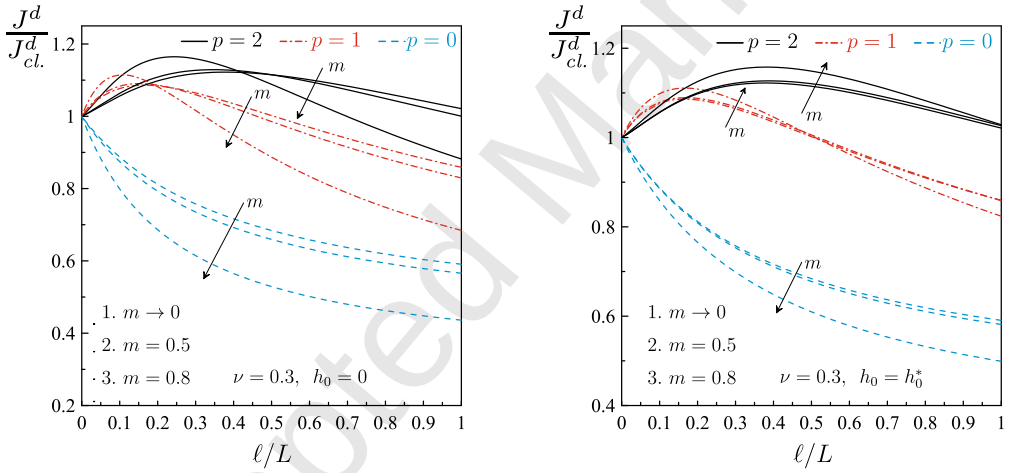

Figure 12: Variation of the ratio of the dynamic ERRs in couple-stress and classical elasticity with respect to the geometric ratio ℓ/L. (**left**) for $h_0 = 0$ (zero micro-inertia) and (**right**) for $h_0 = h_0^*$. The Poisson's ratio is $\nu = 0.3$, and $h_0^* = 1.078$.

been observed also experimentally in fracture of ceramic materials under remote loading where a decrease in the ERR takes place as the length of the crack becomes comparable to the grain size ([60, 11, 12]). A qualitative different behavior is observed for loading profiles with $p > 0$, in such cases the ratio of the ERRs may increase *above* unity in a range of values of ℓ/L which depends upon the parameters: m, h_0, and p. Higher values of these parameters implies a larger range of ℓ/L at which $J^d/J^d_{cl.} > 1$. The latter finding shows that the couple-stress theory may predict also a *weakening* effect, where more energy needs to be provided with respect to a classical elastic material in order for the crack to advance further. A similar behavior was observed in the interaction problem of a glide dislocation and a shear crack in the context of couple-stress elasticity (Baxevanakis et al. [61]) and in the case of a mode II semi-infinite crack under

concentrated static loading (Gourgiotis et al. [55]).

6. Conclusions

In the present work, we examined the propagation characteristics of shear cracks in microstructured brittle materials modeled by the constrained Cosserat elasticity theory. The dynamic constrained Cosserat theory introduces two characteristic material lengths for isotropic materials that can be related to the intrinsic material microstructure. It was assumed that the crack propagates at a constant sub-Rayleigh speed. The main goal was to investigate the effect of different loading profiles in the macroscopic response of the cracked material, extending thus the recent results presented by Gourgiotis and Piccolroaz [28]. Rotational microinertia effects were also considered in our study since previous experience with couple-stress analyses of surface waves and anti-plane crack problems showed that this term is important, especially at high frequencies. An exact closed form solution of the boundary value problem was obtained by using an integral transform analysis and the Wiener-Hopf technique.

Our results differ in several important respects from the predictions of standard LEFM. It was shown that both the loading type and the microstructural parameters (ℓ, h) strongly influence the fracture process near a rapidly moving shear crack. Our analysis showed that depending on the values of the microstructural ratio $h_0 = h/\ell$, the actual limiting crack speed under in-plane shear loading conditions can be significantly lower than the classical limiting Rayleigh wave speed predicted by the standard elastodynamic theory. This finding is in agreement with the experimental results regarding the limiting velocity during shear fault propagation and sheds light on the effects of the microstructure in dynamic brittle fracture. Moreover, for the steady-state crack propagation problem examined here, it was found that both the SIF and the ERR (J-integral) depend upon the crack velocity. As the crack speed approaches the pertinent Rayleigh velocity both quantities increase significantly but remain, contrary to the classical case, always *finite*. A strengthening effect was observed when the resultant force of the applied loading is localized near the crack-tip. In this case, the ERR decreases monotonically with increasing values of the ratio of the characteristic material length ℓ over the pertinent geometrical length L. This decrease in the crack driving force shows that the microstructure shields the crack tip. Similar strengthening effects have been observed in ceramics when the grain size becomes comparable to the crack length. Conversely, as the profile of the applied loading becomes more uniformly distributed away from the tip of the crack weakening effects are observed. In that case, the ERR predicted by the present theory becomes higher than the classical one showing that a greater amount of energy is provided for the crack to propagate. Finally, it is worth noting that when the characteristic lengths of the theory become vanishingly small, size effects are not observed and the classical result for the ERR is recovered.

Based on our results, we conclude that the constrained Cosserat elasticity

theory, which is the simplest gradient type generalized continuum theory, provides a more accurate and detailed description of the physical mechanisms governing the fracture process of microstructured materials.

Appendix A The classical elasticity solution

For a steady-state propagating crack the governing equations in terms of Lamé potentials assume the following form in the moving coordinate system

$$(1-m^2c^2)\frac{\partial^2\phi}{\partial X^2}+\frac{\partial^2\phi}{\partial Y^2}=0, \quad (1-m^2)\frac{\partial^2\psi}{\partial X^2}+\frac{\partial^2\psi}{\partial Y^2}=0. \tag{A.1}$$

Accordingly, for the mode II case, the pertinent boundary conditions are given in (18), (19), and (21). Note that the stress tensor in this case is symmetric. An exact solution to the boundary value problem described above is obtained using the Fourier transform and the Wiener-Hopf technique. The unilateral Fourier transforms of the unknown stress $\sigma_{yx}(X>0, Y=0)$ ahead of the crack tip, and the unknown crack-face displacement $u_x(X<0, Y=0)$ are defined in (23). Following the procedure outlined in Section 4, the final form of the Wiener-Hopf equation reads

$$\Sigma^+(s)\,[s]_+^{1/2}-T_0H^+(s)=-\frac{\mu R(m)s^2}{m^2(1-m^2)^{1/2}[s]_-^{1/2}}U^-(s)+T_0H^-(s)\equiv E(s) \tag{A.2}$$

with

$$H^+(s)=(-s_0)^{p+1}\left[[s]_+^{1/2}-\sum_{j=0}^{p}F_j(s-s_0)^j\right](s-s_0)^{-p-1}, \tag{A.3}$$

$$H^-(s)=(-s_0)^{p+1}\sum_{j=0}^{p}F_j(s-s_0)^{j-p-1} \tag{A.4}$$

and

$$F_j=\frac{1}{2\pi i}\oint_C\frac{[s]_+^{1/2}}{(s-s_0)^{j+1}}ds=\frac{\sqrt{\pi}s_0^{\frac{1}{2}-j}}{2j!\Gamma(3/2-j)}, \tag{A.5}$$

where C is an arbitrary contour centered at the point $s_0=i/L$ and lying in the analyticity domain. Note that $H^+(s)$ is analytic in $\mathrm{Im}(s)>0$, whereas $H^-(s)$ is analytic in $\mathrm{Im}(s)<L^{-1}$. Moreover, the functions $H^+(s)$ and $H^-(s)$ exhibit the following asymptotic behavior: $H^{\pm}(s)=O(1)$ as $|s|\to 0$ and $H^{\pm}(s)=O(s^{-1})$ as $|s|\to\infty$.

The functional equation (A.2) defines $E(s)$ only on the real line. Taking into account the near-tip asymptotic behavior of the stress and displacement field in classical LEFM and invoking Liouville's theorem, we conclude that $E(s)=T_0E_0$.

The constant E_0 is evaluated by simple equilibrium considerations as in the couple-stress case. In fact, it can be shown that

$$E_0 = \sum_{j=0}^{p} (-s_0)^j F_j = \frac{(1+i)\,\Gamma(1/2+p)}{\sqrt{2\pi L}\,\Gamma(1+p)}, \tag{A.6}$$

In light of the above results, the near-tip behavior of the shear traction and the sliding displacement is found to be

$$\sigma_{yx}(X \to +0, Y=0) = \frac{T_0 \Gamma(1/2+p)}{\pi\sqrt{L}\,\Gamma(1+p)}\, X^{-1/2}, \quad X>0, \tag{A.7}$$

$$u_x(X \to -0, Y=0) = \frac{2T_0 m^2 \sqrt{1-m^2}\Gamma(1/2+p)}{\mu\pi\sqrt{L}\,R(m)\,\Gamma(1+p)}\, (-X)^{1/2}, \quad X<0. \tag{A.8}$$

Further, the stress intensity factor becomes

$$K_{\mathrm{II}}^{d_{cl.}} = \lim_{X\to 0} \sqrt{2\pi X}\,\sigma_{yx}(X, Y=0) = \frac{T_0\sqrt{2}\Gamma(1/2+p)}{\sqrt{\pi L}\,\Gamma(1+p)}. \tag{A.9}$$

Finally, employing the asymptotic relations in (A.7) and (A.8), the classical ERR takes the following form

$$J_{cl.}^{d} = -2 \lim_{\varepsilon\to+0} \int_{-\varepsilon}^{\varepsilon} \sigma_{yx}(X,+0)\cdot \frac{\partial u_x(X,+0)}{\partial X} dX = \frac{T_0^2 m^2 \sqrt{1-m^2}\,\Gamma(1/2+p)^2}{\mu\pi L\,R(m)\,\Gamma(1+p)^2}. \tag{A.10}$$

References

[1] E. Arzt, Size effects in materials due to microstructural and dimensional constraints: a comparative review, Acta Mater. 46 (1998) 5611–5626.

[2] R. Maranganti, P. Sharma, Length scales at which classical elasticity breaks down for various materials, Phys. Rev. Lett. 98 (2007) 195504.

[3] E. Bouchbinder, T. Goldman, J. Fineberg, The dynamics of rapid fracture: instabilities, nonlinearities and length scales, Reports on Progress in Physics 77 (2014) 046501.

[4] J. Fineberg, E. Bouchbinder, Recent developments in dynamic fracture: some perspectives, Int. J. Fract. 196 (2015) 33–57.

[5] R. Rice, S. Freiman, P. Becher, Grain-size dependence of fracture energy in ceramics: I, experiment, J. Am. Ceram. Soc. 64 (1981) 345–350.

[6] Z. Bazant, J. Planas, Fracture and size effect in concrete and other quasibrittle materials, CRC press, 1997.

[7] J. Rice, New perspectives on crack and fault dynamics, in: Mechanics for a New Mellennium, Springer, 2001, pp. 1–24.

[8] N. Lapusta, Y. Liu, Three-dimensional boundary integral modeling of spontaneous earthquake sequences and aseismic slip, J. Geophys. Res. Solid Earth 114 (B9).

[9] C. Yu, A. Pandolfi, M. Ortiz, D. Coker, A. Rosakis, Three-dimensional modeling of intersonic shear-crack growth in asymmetrically loaded unidirectional composite plates, Int. J. Solids Struct. 39 (2002) 6135–6157.

[10] H. Hirakata, O. Nishijima, N. Fukuhara, T. Kondo, A. Yonezu, K. Minoshima, Size effect on fracture toughness of freestanding copper nano-films, Mater. Sci. Eng. A 528 (2011) 8120–8127.

[11] J. Seidel, N. Claussen, J. Rödel, Reliability of alumina ceramics: effect of grain size, J. Eur. Cer. Soc. 15 (1995) 395–404.

[12] O. Tokariev, L. Schnetter, T. Beck, J. Malzbender, Grain size effect on the mechanical properties of transparent spinel ceramics, J. Eur. Cer. Soc. 33 (2013) 749–757.

[13] J. Rakow, A. Waas, Size effects and the shear response of aluminum foam, Mech. Mater. 37 (2005) 69–82.

[14] P. Murali, T. Guo, Y. Zhang, R. Narasimhan, Y. Li, H. Gao, Atomic scale fluctuations govern brittle fracture and cavitation behavior in metallic glasses, Phys. Rev. Lett. 107 (2011) 215501.

[15] D. Owen, Elasticity with gradient-disarrangements: A multiscale perspective for strain-gradient theories of elasticity and of plasticity, J. Elast. 127 (2017) 115–150.

[16] L. Deseri, D. Owen, Toward a field theory for elastic bodies undergoing disarrangements, J. Elast. 70 (2003) 197–236.

[17] L. Deseri, D. Owen, Stable disarrangement phases arising from expansion/contraction or from simple shearing of a model granular medium, Int. J. Eng. Sci. 96 (2015) 111–130.

[18] R. Toupin, Elastic materials with couple-stresses, Arch. Ration. Mech. Anal. 11 (1962) 385–414.

[19] R. Mindlin, H. Tiersten, Effects of couple-stresses in linear elasticity, Arch. Ration. Mech. Anal. 11 (1962) 415–448.

[20] W. Koiter, Couple stresses in the theory of elasticity, I and II, Proc. K. Ned. Akad. Wet. (B) 67 (1964) 17–44.

[21] R. Lakes, Size effects and micromechanics of a porous solid, J. Mat. Sci. 18 (1983) 2572–2580.

[22] W. Anderson, R. Lakes, Size effects due to cosserat elasticity and surface damage in closed-cell polymethacrylimide foam, J. Mat. Sci. 29 (1994) 6413–6419.

[23] D. Bigoni, W. Drugan, Analytical derivation of cosserat moduli via homogenization of heterogeneous elastic materials, J. Appl. Mech. 74 (2007) 741–753.

[24] R. Mora, A. Waas, Evaluation of the micropolar elasticity constants for honeycombs, Acta Mech. 192 (2007) 1.

[25] G. Mishuris, A. Piccolroaz, E. Radi, Steady-state propagation of a mode III crack in couple stress elastic materials, Int. J. Eng. Sci. 61 (2012) 112–128.

[26] A. Piccolroaz, G. Mishuris, E. Radi, Mode III interfacial crack in the presence of couple-stress elastic materials, Eng. Fract. Mech. 80 (2012) 60–71.

[27] L. Morini, A. Piccolroaz, G. Mishuris, E. Radi, On fracture criteria for dynamic crack propagation in elastic materials with couple stresses, Int. J. Eng. Sci. 71 (2013) 45–61.

[28] P. Gourgiotis, A. Piccolroaz, Steady-state propagation of a mode II crack in couple stress elasticity, Int. J. Fract. 188 (2) (2014) 119–145.

[29] L. Morini, A. Piccolroaz, G. Mishuris, Remarks on the energy release rate for an antiplane moving crack in couple stress elasticity, Int. J. Solids Struct. 51 (2014) 3087–3100.

[30] A. Dyskin, E. Pasternak, Asymptotic analysis of fracture propagation in materials with rotating particles, Eng. Fract. Mech. 150 (2015) 1–18.

[31] H. Yu, T. Sumigawa, T. Kitamura, M. Kuna, Domain-independent I-integrals for force and couple stress intensity factor evaluations of a crack in micropolar thermoelastic medium, Int. J. Solids Struct. 100 (2016) 470–484.

[32] T. Zisis, P. Gourgiotis, F. Dal Corso, A contact problem in couple stress thermoelasticity. the indentation by a hot flat punch, Int. J. Solids Struct. 63 (2015) 226–239.

[33] P. Gourgiotis, T. Zisis, K. Baxevanakis, Analysis of the tilted flat punch in couple-stress elasticity, Int. J. Solids Struct. 85 (2016) 34–43.

[34] A. Karuriya, T. Bhandakkar, Plane strain indentation on finite thickness bonded layer in couple stress elasticity, Int. J. Solids Struct. 108 (2017) 275–288.

[35] P. Gourgiotis, D. Bigoni, Stress channelling in extreme couple-stress materials part I: Strong ellipticity, wave propagation, ellipticity, and discontinuity relations, J. Mech. Phys. Solids 88 (2016) 150–168.

[36] P. Gourgiotis, D. Bigoni, Stress channelling in extreme couple-stress materials part II: Localized folding vs faulting of a continuum in single and cross geometries, J. Mech. Phys. Solids 88 (2016) 169–185.

[37] D. Bigoni, P. Gourgiotis, Folding and faulting of an elastic continuum, Proc. R. Soc. Lond. A 472 (2187) (2016) 20160018.

[38] T. Zisis, Anti-plane loading of microstructured materials in the context of couple stress theory of elasticity: half-planes and layers, Arch. Appl. Mech. (2017) 1–14.

[39] A. Piccolroaz, A. Movchan, Dispersion and localisation in structured rayleigh beams, Int. J. Solids Struct. 51 (2014) 4452–4461.

[40] A. Goodarzi, M. Fotouhi, H. Shodja, Inverse scattering problem of reconstruction of an embedded micro-/nano-size scatterer within couple stress theory with micro inertia, Mech. Mater. 103 (2016) 123–134.

[41] C. Wang, P. Wei, P. Zhang, Y. Li, Influences of a visco-elastically supported boundary on reflected waves in a couple-stress elastic half-space, Archives of Mechanics 69 (2017) 131–156.

[42] P. Gourgiotis, D. Bigoni, The dynamics of folding instability in a constrained Cosserat medium, Phil. Trans. R. Soc. Lond. A 375(2093) (2017) 20160159.

[43] D. Gazis, R. Herman, R. Wallis, Surface elastic waves in cubic crystals, Physical Review 119 (1960) 533.

[44] H. Georgiadis, E. Velgaki, High-frequency Rayleigh waves in materials with micro-structure and couple-stress effects, Int. J. Solids Struct. 40 (2003) 2501–2520.

[45] R. Mindlin, Micro-structure in linear elasticity, Arch. Ration. Mech. Anal. 16 (1964) 51–78.

[46] S. P. Filopoulos, T. K. Papathanasiou, S. I. Markolefas, G. J. Tsamasphyros, Dynamic finite element analysis of a gradient elastic bar with micro-inertia, Comp. Mech. 45 (2010) 311–319.

[47] T. K. Papathanasiou, P. A. Gourgiotis, F. Dal Corso, Finite element simulation of a gradient elastic half-space subjected to thermal shock on the boundary, Appl. Math. Model. 40 (2016) 10181–10198.

[48] R. Lakes, Dynamical study of couple stress effects in human compact bone, J. Biomech. Eng 104 (1982) 6–11.

[49] C. Chen, R. Lakes, Dynamic wave dispersion and loss properties of conventional and negative Poisson's ratio polymeric cellular materials, Cell. Polym. 8 (1989) 343–359.

[50] C. Thomas, S. Papargyri-Beskou, G. Mylonakis, Wave dispersion in dry granular materials by the distinct element method, Soil Dyn. Earthq. Eng. 29 (2009) 888–897.

[51] V. Erofeev, V. Rodyushkin, J. Wood, Observation of the dispersion of elastic waves in a granular composite and a mathematical model for its description, Sov. Phys. Acoust. 38 (1992) 611–612.

[52] A. Kondratev, Precision-measurements of the velocity and attenuation of ultrasound in solids, Sov. Phys. Acoust. 36 (1990) 470–476.

[53] J. Jia, Modern earthquake engineering, Springer, 2017.

[54] L. Freund, Dynamic fracture mechanics, Cambridge University Press, 1998.

[55] P. Gourgiotis, H. Georgiadis, M. Sifnaiou, Couple-stress effects for the problem of a crack under concentrated shear loading, Math. Mech. Solids 17 (2012) 433–459.

[56] E. Sternberg, R. Muki, The effect of couple-stresses on the stress concentration around a crack, Int. J. Solids Struct. 3 (1967) 69–95.

[57] H. Georgiadis, The mode III crack problem in microstructured solids governed by dipolar gradient elasticity: static and dynamic analysis, ASME J. Appl. Mech. 70 (2003) 517–530.

[58] S. Kulakhmetova, V. Saraikin, L. Slepyan, Plane problem of a crack in a lattice, Mech. Solids 19 (1984) 102–108.

[59] M. Nieves, A. Movchan, I. Jones, G. Mishuris, Propagation of slepyan's crack in a non-uniform elastic lattice, J. Mech. Phys. Solids 61 (2013) 1464–1488.

[60] R. Rice, S. Freiman, J. Mecholsky, The dependence of strength-controlling fracture energy on the flaw-size to grain-size ratio, J. Am. Ceram. Soc. 63 (1980) 129–136.

[61] K. Baxevanakis, P. Gourgiotis, H. Georgiadis, Interaction of cracks with dislocations in couple-stress elasticity. Part II: Shear modes, Int. J. Solids Struct. 118-119 (2017) 192 – 203.